

# Vaporization of liquid droplet with large deformation and high mass transfer rate, I: Constant-density, constant-property case

Yanxing Wang, Vigor Yang\*

School of Aerospace Engineering, Georgia Institute of Technology, Atlanta, GA 30332, USA

## ARTICLE INFO

### Article history:

Received 20 August 2017  
 Received in revised form 9 March 2019  
 Accepted 13 March 2019  
 Available online 15 April 2019

### Keywords:

Liquid droplet vaporization  
 Droplet deformation  
 Interface localization

## ABSTRACT

A numerical model based on decomposed vaporization mechanisms has been developed for the study of vaporization of liquid droplets with large deformation and high mass transfer rate. In this model, the vaporization-induced volume, energy, and species source terms in the gas phase are modeled using a body-fitted layer placed around the interface on the gas side. In this layer, continuous distributions of volume, energy, and species sources are specified by the conservation laws. A corresponding body-fitted sink layer is placed on the liquid side of the interface to account for mass, energy and species loss in the liquid phase due to vaporization. The formulation retains the advantages of interface localization methods and mitigates the error and complexity caused by the combined treatment of mass/heat transfer and interface localization. The new model is versatile and does not depend on the specific interface localization method, and can thus be implemented in any of the existing methods. As a specific example, the present approach is implemented in a volume-of-fluid (VOF)-based code "Gerris". A number of test cases concerning liquid vaporization in both quiescent and convective environments are presented, with the constant-density assumption, to verify and validate this model in terms of interface localization. In particular, the vaporization of a single *n*-decane droplet in a uniform air flow of 1000 K at 1 atm is investigated. The predicted liquid volume evolution demonstrates the robustness and accuracy of interface localization for cases with large density ratio and high vaporization rate. Vaporization of *n*-decane droplets with large deformation and high mass transfer is also investigated systematically.

© 2019 Elsevier Inc. All rights reserved.

## 1. Introduction

Heat and mass transfer across the deforming interface in a multiphase flow is of great importance in a wide range of engineering and scientific applications, including the vaporization of droplets in the combustion of fuel sprays in energy conversion systems. The details of such interfacial deformation and vaporization, however, remain largely unknown, mainly due to challenges in conducting quantitative analysis and making experimental measurements with sufficient resolution.

Numerical simulations of multiphase flows with deformable interface have received considerable attention in the past decades. Several techniques have been developed and applied to a variety of problems with reasonable success. These include the volume-of-fluid (VOF) [1,2], level-set [3,4], and front tracking [5,6] methods. For situations involving mass transfer, many challenges, however, remain unresolved. Stefan flow caused by mass transfer creates an abrupt change in normal ve-

\* Corresponding author.

E-mail address: vigor.yang@aerospace.gatech.edu (V. Yang).

licity across the two-phase interface, which in turn causes a number of difficulties in modeling the vaporization process in a continuous manner. The challenges include: localization of the interfacial boundary, estimation of temperature and species concentrations at the interface, calculation of gas and liquid velocities near the interface, coupling of heat and mass transfer, and treatment of density variation caused by strong temperature change near the interface.

Most existing methods dealing with mass transfer across the interface were developed based on the aforementioned interface localization methods [1–6]. For example, Welch and Wilson [7], Sato et al. [8], and Schlottke and Weigand [9] utilized VOF-based methods for constant-density boiling flows; Son and Dhir [10], and Gibou et al. [11] developed level-set based methods for evaporating two-phase flows; Juric and Tryggvason [12] and Esmaeeli and Tryggvason [13] employed front-tracking methods for boiling flows; and Hardt and Wondra [14] presented a vaporization model independent of any specific realization of interface localization scheme. These methods treat mass transfer across the two-phase interface in a continuous manner by enforcing a divergence constraint in grid cells containing the interface, and calculate the interface velocity according to the conservation of mass. The disadvantages of such treatment lie in the potential inaccuracy of interface localization in flows with a large density ratio and a high mass transfer rate; such conditions create a sharp velocity jump across the interface and can easily cause a nonphysical shift of the interface in the simulation. Furthermore, the calculation of flow velocity in grid cells containing the interface requires very complex treatments, thereby posing additional implementation challenges. All of the issues arise from the concurrent treatment of interface localization and mass transfer across the interface in the same grid cells. These challenges have prompted us to develop a numerical model in which the mass transfer and interface localization can be treated separately, while preserving the advantages of interface localization methods.

In this paper, we present a method based on a unified treatment of the gas and liquid phases in the vaporization process. The method takes into account the vaporization-induced variations of volume, energy, and species concentrations in the gas phase by considering a body-fitted source layer placed around the interface on the gas side. In this layer, a continuous distribution of volume, energy, and species sources is specified according to the conservation laws. A corresponding body-fitted sink layer is placed near the interface on the liquid side to account for the mass, energy, and species loss in the liquid phase. The two layers allow us to separate the treatment of heat and mass transfer across the interface from that of interface localization. The velocity jump across the interface in real physics is artificially moved to the source layer and distributed over the layer thickness. At the same time, the sink layer in the liquid phase causes a volume reduction in the vicinity of the interface, which causes the interface to regress, to account for the volume loss of the liquid phase due to vaporization. In the region spanning the source and sink layers, the velocity changes smoothly across the interface over a few grid cells. The model effectively preserves the advantages of interface localization methods and circumvents the error and complexity caused by the combined treatment of mass/heat transfer and surface localization. The new model is versatile and does not depend on the specific interface localization method, and can thus be implemented in any of the existing approaches. Although only cases with a single-component liquid are considered in this paper, the proposed vaporization model can be extended to situations with multi-component liquids by taking into account fluid property variations associated with species concentration changes [15].

In the present work, we take advantage of the well-developed VOF based code “Gerris” [16,17] and use a single *n*-decane droplet in air as an example, to demonstrate the development of the model and examine its accuracy and capabilities. Gerris is an open-source software program developed by Stéphane Popinet [16,17] for incompressible multi-phase flows. It employs an adaptive mesh projection method to solve the time-dependent incompressible Navier-Stokes equations, and uses the VOF approach to capture interfacial evolution. Gerris has second-order spatio-temporal accuracy on both static and dynamic grids in various flow conditions [16,17].

## 2. Mathematical formulation and numerical methods

In liquid vaporization with high mass transfer driven by a large temperature difference between the gas and liquid phases, gas properties such as density, viscosity, and thermal conductivity vary considerably near the interface, because of the abrupt changes of temperature and species concentrations. Moreover, the thermal expansion of evaporated liquid adds additional velocity to the gas flow. Neglecting such variations and treating the flow as incompressible may cause errors in the prediction. As the first step of our series of model developments, we construct the present work based on the constant-density assumption, similar to other studies [7–13]. All the properties in the gas phase are considered constant and are evaluated using the well-known “1/3 rule” suggested by Yuen and Chen [18]. The reference temperature and vapor mass fraction for evaluating the gas properties are,

$$T_{ref} = T_s + \frac{1}{3}(T_\infty - T_s), \quad \text{and} \quad Y_{ref} = Y_s + \frac{1}{3}(Y_\infty - Y_s), \quad (1)$$

where the subscripts “s” and “∞” denote the properties at the droplet surface and in the far field, respectively. The temperature and vapor mass fraction at the interface need to be estimated in advance. In this work, we use the values of a single droplet in a quiescent environment, which can be acquired from the classical 1-D evaluation with quasi-steady assumption, as an approximation to estimate  $T_{ref}$  and  $Y_{ref}$ .

We consider the two-phase flow as incompressible and continuous in both phases. The conservation equations of mass, momentum, energy, and species mass fraction are given as

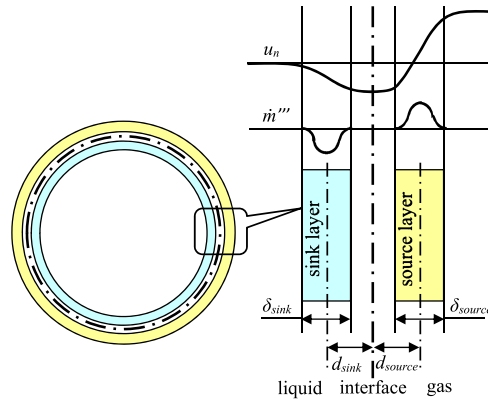


**Fig. 1.** Vaporization model based on the decomposed mechanisms. (For interpretation of the colors in the figure(s), the reader is referred to the web version of this article.)

$$\nabla \cdot \mathbf{u} = \frac{\dot{m}'''}{\rho} \quad (2)$$

$$\frac{\partial \mathbf{u}}{\partial t} + \mathbf{u} \cdot \nabla \mathbf{u} = -\frac{1}{\rho} \nabla p + \nu \nabla^2 \mathbf{u} + \sigma \kappa \delta_s \mathbf{n} \quad (3)$$

$$\frac{\partial T}{\partial t} + \mathbf{u} \cdot \nabla T = \frac{k}{\rho c_p} \nabla^2 T + \frac{1}{\rho c_p} \dot{m}''' \Delta h_{fg} \quad (4)$$

$$\frac{\partial Y_{vap}}{\partial t} + \mathbf{u} \cdot \nabla Y_{vap} = D_m \nabla^2 Y_{vap} + \frac{\dot{m}'''}{\rho} \quad (5)$$

where  $\rho$  is the density,  $\mathbf{u}$  the velocity vector,  $T$  the temperature,  $\Delta h_{fg}$  the enthalpy of vaporization,  $Y_{vap}$  the mass fraction of vapor.  $\dot{m}'''$  is the mass production rate per unit volume due to vaporization, and is nonzero only in the source and sink layers around the interface. In the momentum equation, surface tension is treated as a continuous body force expressed as  $\sigma \kappa \delta_s \mathbf{n}$ , where  $\sigma$  is the surface tension of the liquid in the gas,  $\kappa$  the interface curvature and  $\delta_s$  the Dirac-delta function. The equation of species mass fraction (Eq. (5)) is only needed in the gaseous phase. All the properties of the gas phase are considered as constant and are evaluated by Eq. (1). We use the VOF approach to capture the spatiotemporal evolution of the two-phase interface. The transport equation for liquid volume fraction  $F$  takes the form

$$\frac{\partial F}{\partial t} + \mathbf{u} \cdot \nabla F = 0. \quad (6)$$

Equations (2)–(6) are solved by a numerical method combining quad/octree discretization, a time-staggered projection method, and a multilevel Poisson solver. More details are given in Popinet [16,17]. The formulation remains unclosed due to the lack of mass production rate  $\dot{m}'''$  in Eq. (2); this will be discussed in the following.

### 3. Vaporization model

In practice, vaporization takes place at the two-phase, zero-thickness interface, and causes a sharp increase in the normal velocity in the gas phase. This velocity discontinuity poses many challenges in interface localization in numerical simulations. In the present model, as shown in Fig. 1, the mass transfer and subsequent normal velocity change across the interface expand over a region of finite thickness around the interface. The region includes a source layer with a positive mass production rate  $\dot{m}'''$  in the gas phase to model the increase in volume, mass, and energy due to vaporization, and a sink layer with a negative mass production rate  $\dot{m}'''$  in the liquid phase to model the loss of volume, mass, and energy in the liquid. The thicknesses of the two layers span several grid cells, and are denoted by  $\delta_{source}$  and  $\delta_{sink}$ , respectively, as shown in Fig. 1. The distances from the center lines of the source and sink layers to the interface are denoted by  $d_{source}$  and  $d_{sink}$ , respectively. The grids near the interface must be dense enough to resolve the source and sink layers and the region between them.

The volume changes in the two phases due to mass transfer are described by Eq. (2). The negative mass production rate in the sink layer ( $\dot{m}'''_{sink} < 0$ ) imparts to fluid between the sink layer and the interface an addition normal velocity toward the liquid phase, and thus pulls the interface toward the liquid phase, to model the interface regression. In the meantime, the positive mass production rate in the source layer ( $\dot{m}'''_{source} > 0$ ) causes an increase in normal velocity in the gas phase, accounting for the Stefan flow in the process of vaporization. The mass conservation in the liquid phase ensures that the interface regression rate is consistent with the vaporization rate. In the region between the source and sink layers, the velocity varies continuously across the interface. The process guarantees the accuracy of interface localization with the

methods mentioned above. Compared with previous vaporization models, the present work does not require any special treatment at the interface, and as such significantly facilitates implementation of the model.

The continuous mass production rates in the source and sink layers are related to the vaporization rate as,

$$\int_{\delta_{source}} \dot{m}'''_{source} dx = - \int_{\delta_{sink}} \dot{m}'''_{sink} dx = \dot{m}'' \tag{7}$$

where  $x$  is the coordinate normal to the interface, with the origin at the center of each layer.  $\dot{m}''$  is the vaporization rate in mass determined by the heat flux to the interface,

$$\dot{m}'' = \frac{1}{\Delta h_{fg}} \left( k_{gas} \frac{\partial T}{\partial n} \Big|_{s,g} - k_{liq} \frac{\partial T}{\partial n} \Big|_{s,l} \right) \tag{8}$$

Here  $\Delta h_{fg}$  is the enthalpy of vaporization. A sinusoidal profile is adopted to describe the mass production rate in the source and sink layers,

$$\begin{cases} \dot{m}'''_{source} = \frac{\dot{m}''}{\delta_{source}} (1 + \cos(2\pi x / \delta_{source})) \\ \dot{m}'''_{sink} = -\frac{\dot{m}''}{\delta_{sink}} (1 + \cos(2\pi x / \delta_{sink})), \end{cases} \tag{9}$$

Equation (8) provides the first link between the energy and species.

Due to the interface curvature and the deviation of the source and sink layers from the interface, the areas of the central surfaces of the source and sink layers are different from that of the interface. This causes errors in the calculation of the mass transfer rate. Hardt and Wondra [14] proposed a spatial-integration treatment to ensure the consistency of mass transfer across the interface. In the present work, we introduce two correction factors for the mass production rates in the source and sink layers, respectively, to compensate for the artificial area change of the layers,

$$\dot{m}''_{source} \equiv \alpha_{source} \dot{m}'' \quad \text{and} \quad \dot{m}''_{sink} \equiv \alpha_{sink} \dot{m}'' \tag{10}$$

and

$$\begin{aligned} \alpha_{source} &= \frac{\Delta S_{interface}}{\Delta S_{source}} = \frac{R_{curv}^2}{(R_{curv} + d_{source})^2} \\ \alpha_{sink} &= \frac{\Delta S_{interface}}{\Delta S_{sink}} = \frac{R_{curv}^2}{(R_{curv} - d_{sink})^2}. \end{aligned} \tag{11}$$

Here  $d_{source}$  and  $d_{sink}$  are the distance of the central surface of the source and sink layers, respectively, from the interface, and  $R_{curv}$  is the radius of curvature of the interface. The method guarantees the conservation of mass. The radius of curvature of the interface is calculated by,

$$R_{curv} = \frac{1}{\nabla \cdot (\nabla F / |\nabla F|)}, \tag{12}$$

where  $F$  is the liquid volume fraction described by Eq. (6).

The energy and mass-fraction equations, Eqs. (4) and (5), are coupled through vaporization, Eq. (8). The surface temperature  $T_s$  is related to the vapor pressure at the interface, according to the Clausius–Clapeyron equation,

$$\ln \frac{p_{vap,s}}{p} = \frac{\Delta h_{fg} M_{vap}}{R_u} \left( \frac{1}{T_{boil}} - \frac{1}{T_s} \right), \tag{13}$$

where  $p_{vap,s}$  is the partial pressure of vapor at the interface,  $p$  the total pressure,  $M_{vap}$  the molecular weight of the vapor species, and  $R_u$  the universal gas constant. This condition makes the interface temperature  $T_s$  slightly lower than the boiling temperature  $T_{boil}$ , a condition known as the pseudo wet-bulb temperature [19]. The vapor partial pressure  $p_{vap,s}$  is related to the vapor mole fraction  $X_{vap,s}$  as

$$p_{vap,s} = X_{vap,s} p \tag{14}$$

Substitution of this expression into the Clausius–Clapeyron equation (Eq. (13)) provides another link between the energy and species balances,

$$\ln X_{vap,s} = \frac{\Delta h_{fg} M_{vap}}{R_u} \left( \frac{1}{T_{boil}} - \frac{1}{T_s} \right) \tag{15}$$

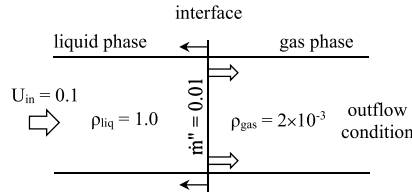


Fig. 2. 1D test case, with mass transfer.

Physically, the vapor mole fraction at the two-phase interface  $X_{vap,s}$  depends on the surface vaporization rate  $\dot{m}''$  and the mass transfer described by Eq. (5). At the same time,  $X_{vap,s}$  couples with  $T_s$  through the Clausius–Clapeyron equation. The energy equation (Eq. (4)) and the species mass fraction equation (Eq. (5)), as well as the links between them, that is, the surface vaporization equation (Eq. (8)) and the Clausius–Clapeyron equation (Eq. (15)), constitute the formulation of liquid vaporization. The strong coupling among all the variables makes the system difficult to solve using explicit schemes. In the past, iteration methods were generally adopted [20], but such methods pose serious computational challenges in terms of efficiency and robustness. To circumvent this problem, we decouple  $X_{vap,s}$  from  $T_s$ , with  $X_{vap,s}$  primarily determined by the surface vaporization rate  $\dot{m}''$  and the mass transfer equation. Then, we use an approximate explicit scheme, summarized as follows, to solve the decoupled equations:

$$\begin{aligned} (\dot{m}'')^{n+1} &= 2(\dot{m}'')^n - (\dot{m}'')^{n-1} \\ &= \frac{2}{\Delta h_{fg}} \left( k_{gas} \frac{\partial T^n}{\partial n} \Big|_{s,g} - k_{liq} \frac{\partial T^n}{\partial n} \Big|_{s,l} \right) - \frac{1}{\Delta h_{fg}} \left( k_{gas} \frac{\partial T^{n-1}}{\partial n} \Big|_{s,g} - k_{liq} \frac{\partial T^{n-1}}{\partial n} \Big|_{s,l} \right) \end{aligned} \quad (16)$$

$$\frac{1}{\Delta t} Y_{vap}^{n+1} = \frac{1}{\Delta t} Y_{vap}^n - \mathbf{u}^{n+1/2} \cdot \nabla Y_{vap}^{n+1/2} + D_m \nabla^2 Y_{vap}^{n+1/2} + \frac{1}{\rho} (\dot{m}''')^{n+1} \quad (17)$$

$$\frac{1}{\Delta t} T^{n+1} = \frac{1}{\Delta t} T^n - \mathbf{u}^{n+1/2} \cdot \nabla T^{n+1/2} + \frac{k}{\rho c_p} \nabla^2 T^{n+1/2} + \frac{1}{\rho c_p} (\dot{m}''')^{n+1} \Delta h_{fg} \quad (18)$$

$$X_{vap,s}^{n+1} = Y_{vap,s}^{n+1} \frac{\bar{M}}{M_{vap}} \quad (19)$$

$$T_s^{n+1} = \left( \frac{1}{T_{boil}} - \frac{R_u}{\Delta h_{fg} M_{vap}} \ln X_{vap,s}^{n+1} \right)^{-1} \quad (20)$$

Equations (16)–(20) are solved successively at each time step. Notice that the surface vaporization rate  $\dot{m}''$  at the current time step is obtained by extrapolating from  $\dot{m}''$  at the last two time steps.

#### 4. Model verification and validation

Considerable verification and validation for the Gerris code has been done on flows without mass transfer, and Gerris has demonstrated powerful capabilities in dealing with multiphase flow with high velocity and strong deformation [21–23]. In the present work, model verification and validation is focused on interface capture in flows with large liquid/gas density ratios and high vaporization rates. The challenges of simulating this kind of flow lie in the interface regression rate, which is low as compared with the high velocity jump across the interface and the strong coupling of thermal and mass transfer near the interface. In this section, two test cases are presented to demonstrate the efficient implementation and reliable solution of the present approach.

##### 4.1. One-dimensional flow with mass transfer

We first examine the accuracy and effectiveness of the interface capturing capability against a one-dimensional case with mass transfer, as illustrated in Fig. 2. In this test example, heat transfer is ignored and all variables are given in a nondimensional form. The liquid and the gas densities are  $\rho_{liq} = 1.0$  and  $\rho_{gas} = 0.002$ , respectively, and the mass transfer rate is  $\dot{m}'' = 0.01$ . The corresponding density ratio is  $\rho_{liq}/\rho_{gas} = 500$ . The interface regression velocity is  $u_s = \dot{m}''/\rho_{liq} = 0.01$ , and the gas velocity relative to the interface is  $u'_{gas} = \dot{m}''/\rho_{gas} = 5$ . The ratio of the relative gas velocity to the interface regression velocity is  $u'_{gas}/u_s = 500$ . The axial velocity in the liquid phase,  $U_{in} = 0.1$ , is ten times the interface regression velocity. Such high density and velocity ratios present a significant challenge to the interface capture method, in addition to the difficulty associated with the finite liquid velocity. Although this case is inherently one-dimensional, the simulations are carried out on a two-dimensional Cartesian grid with periodic boundary conditions at the upper and lower boundaries of the domain.

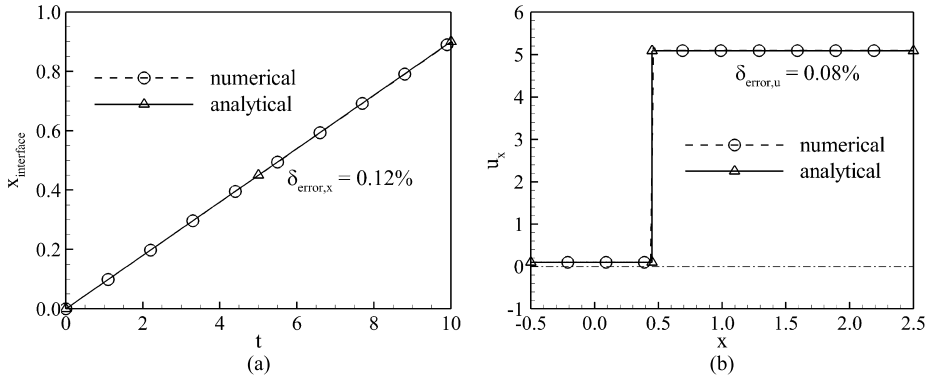


Fig. 3. Numerical and analytical results for 1D test case: (a) Temporal evolution of interface position; (b) Spatial distribution of axial velocity at  $t = 5$ .

**Table 1**  
Properties of gas and liquid.

	$\rho$ (kg/m <sup>3</sup> )	$\nu$ (m <sup>2</sup> /s)	$K$ (kJ/s-m-k)	$c_p$ (kJ/kg-K)	$\alpha$ (m <sup>2</sup> /s)	$D_m$ (m <sup>2</sup> /s)
Liquid	604.14	$0.335 \times 10^{-6}$	$0.949 \times 10^{-4}$	2.81	$5.59 \times 10^{-8}$	NA
Gas	1.03	$45.71 \times 10^{-6}$	$0.466 \times 10^{-4}$	2.15	$2.11 \times 10^{-5}$	$1.93 \times 10^{-5}$

Fig. 3 shows the temporal evolution of the interface position  $x_{\text{int}}$  and the spatial distribution of the axial velocity at  $t = 5$ . Both the numerical simulation and the analytical result are presented. The interface travels with the liquid at  $U_{\text{in}} = 0.1$ . At the same time, it regresses to the liquid at  $u'_s = -0.01$  because of mass transfer. The compound interface velocity thus becomes  $u_s = u_{\text{liq}} + u'_s = 0.09$ . The relative deviation between the numerical and analytical simulations is  $\delta_{\text{error},x} \equiv |x_{\text{int,num}} - x_{\text{int,anal}}|/x_{\text{int,anal}} = 0.12\%$ . The liquid velocity should remain constant at the entrance velocity. At the interface, the velocity jumps abruptly, due to the phase change. In our model, the interface is expanded over a banded region of finite thickness, across which the velocity changes continuously. The gas velocity can be estimated as the interface velocity plus the relative velocity of the gas,  $u_{\text{gas}} = u_s + u'_{\text{gas}} = 5.09$ . Compared with this analytical result, the relative error of the gas velocity from the numerical simulation becomes  $\delta_{\text{error},u} \equiv |u_{x,\text{num}} - u_{x,\text{anal}}|/u_{x,\text{anal}} = 0.08\%$ . The small error corroborates the accuracy and robustness of the present method for interface localization for two-phase flows with large density ratios.

#### 4.2. Vaporization of *n*-decane droplet in air flow

The experiment of Wong and Lin [24] provides measurements of the size and temperature evolution of an *n*-decane droplet in air, and this allows for careful validation of the present model under high vaporization conditions. In their experiment, a spherical droplet with an initial size of  $D_0 = 1.98$  mm and an initial temperature of  $T_{d,0} = 315$  K was suspended in a hot air flow with  $T_{\text{air}} = T_{\infty} = 1000$  K and  $U_{\text{air}} = 1$  m/s at one atmosphere. We estimated the gas-phase properties at the reference temperature and mass fraction calculated by Eq. (1) according to the 1/3 rule. The surface temperature  $T_s$  is approximated by the boiling point,  $T_{\text{boil}} = 447$  K. The reference temperature  $T_{\text{ref}}$  thus becomes

$$T_{\text{ref}} \approx T_{\text{boil}} + \frac{1}{3}(T_{\infty} - T_{\text{boil}}) = 631.3 \text{ K} \quad (21)$$

A quasi-steady assumption is made for droplet vaporization in quiescent air, giving the vapor mass fraction at the interface  $Y_s = 0.794$ . Assuming  $Y_{\infty} = 0$ , we obtain the reference vapor mass fraction as follows,

$$Y_{\text{ref}} = Y_s + \frac{1}{3}(Y_{\infty} - Y_s) = 0.574 \quad (22)$$

Table 1 lists the estimated gas- and liquid-phase properties. The density ratio is  $\rho_{\text{liq}}/\rho_{\text{gas}} \approx 600$ , and the temperature difference  $\Delta T = T_{\infty} - T_s \approx 553$  K.

In the simulation, the thicknesses of the source and sink layers are taken to be  $\delta_{\text{source}} = \delta_{\text{sink}} = (1/35)R_0$ , and their distance from the interface is  $d_{\text{source}} = d_{\text{sink}} = (1/20)R_0$ , where  $R_0$  is the droplet radius. Physically, the smaller the layer thickness  $\delta_{\text{source}} \& \text{sink}$  and the smaller the layer distance  $d_{\text{source}} \& \text{sink}$ , the closer the model is to the real situation. We compare the temperature gradients at the interface between simulations with  $\delta_{\text{source}} \& \text{sink} = (1/35)R_0$ ,  $d_{\text{source}} \& \text{sink} = (1/20)R_0$  and  $\delta_{\text{source}} \& \text{sink} = (1/18)R_0$ ,  $d_{\text{source}} \& \text{sink} = (1/10)R_0$ . The relative difference is less than 3%. The selection of  $\delta_{\text{source}} \& \text{sink}$  and  $d_{\text{source}} \& \text{sink}$  will primarily be determined according to the accuracy requirement of a specific work and the affordability of computer resources.

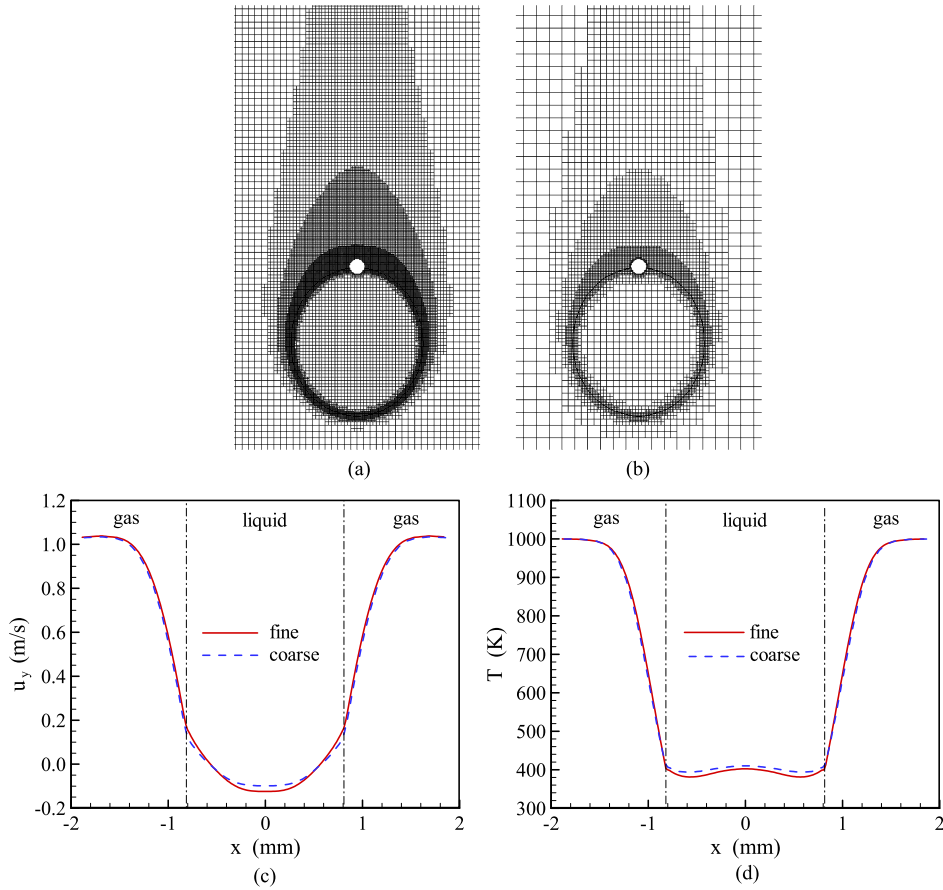


**Fig. 4.** Effect of grid resolution on streamwise velocity and temperature for vaporization of suspended *n*-decane droplet in a uniform airflow at  $t = 2$  s: (a) fine grids with  $\Delta_{\min} = 0.01R_{d,0}$ ; (b) coarse grids with  $\Delta_{\min} = 0.02R_{d,0}$ ; (c) streamwise velocity and (d) temperature on cross section through droplet center.

#### 4.2.1. Grid independence study

An adaptive mesh refinement algorithm is used to dynamically resolve the flow characteristics according to the spatial gradients of temperature and vapor mass fraction. To examine the grid sensitivity of the numerical result, simulations were conducted with two sets of meshes: fine mesh with  $\Delta_{\min} = 0.01R_0$  and coarse mesh  $\Delta_{\min} = 0.02R_0$ , where  $\Delta_{\min}$  is the minimum size of mesh cells and  $R_0$  the initial droplet radius. Fig. 4 shows two different meshes and the corresponding distributions of streamwise velocity and temperature on the cross section through the droplet center at  $t = 2$  s. At each level of the controlling variables (the spatial gradients of temperature and vapor mass fraction), the size of the coarse grid is twice that of the fine grid. Excellent convergence between the results with both coarse and fine grids is obtained, but in the present study the fine mesh is used for all cases to ensure the accuracy of numerical simulations. The detailed patterns of flow and temperature will be discussed in Section 4.2.4.

#### 4.2.2. Heating of *n*-decane droplet in quiescent fluid

Before studying the case of droplet vaporization, we first examine the heating of an *n*-decane droplet at  $T_{d,0} = 315$  K in a quiescent ambient fluid at  $T_{\text{amb}} = T_{\text{boil}} = 447$  K. The droplet diameter is the same as that in Wong and Lin's experiment [24]. The computational domain is 10 times larger than the droplet size. In order to obtain the analytical solution, the properties of the ambient fluid are taken to be the same as those of the *n*-decane droplet, as given in Table 1. The energy equation is solved in spherical coordinates by means of the method of separation of variables, giving the temperature evolution of the droplet and the ambient fluid as follows,

$$T(r, t) = T_{\text{cnt}} + \sum_{i=1}^{\infty} \frac{C_i}{r} \sin\left(\frac{i\pi r}{R_{\text{cnt}}}\right) \exp\left[-\alpha_{\text{liq}} \left(\frac{i\pi}{R_{\text{cnt}}}\right)^2 t\right] \quad (23)$$

where

$$C_i(r, t) = -2 \frac{(T_{d,0} - T_{\text{cnt}})}{i\pi} \left[ R_d \cos\left(\frac{i\pi R_d}{R_{\text{cnt}}}\right) - \left(\frac{R_{\text{cnt}}}{i\pi}\right) \sin\left(\frac{i\pi R_d}{R_{\text{cnt}}}\right) \right] \quad (24)$$

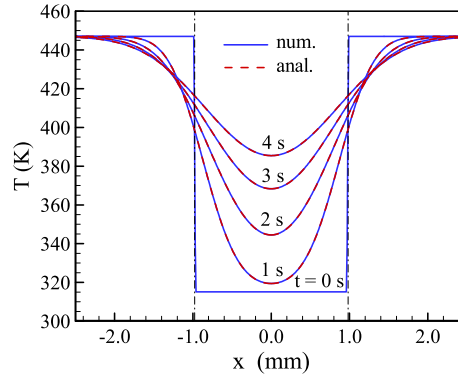


Fig. 5. Temperature evolution of numerical and analytical results for *n*-decane droplet heating in quiescent fluid with same properties.

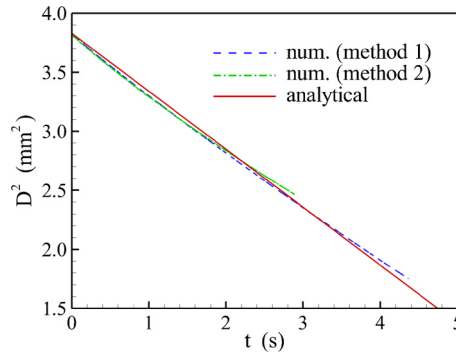


Fig. 6. Temporal evolution of square of *n*-decane droplet diameter in quiescent air ( $T_{air} = 1000$  K).

$R_d$  is the droplet radius,  $R_{cnt}$  the radius of the computational domain, and  $\alpha_{liq}$  the thermal diffusivity of liquid *n*-decane.

In Fig. 5 we compare the temperature distribution from the numerical simulation and the analytical solution. At  $t = 0$  s, temperature decreases sharply from the uniform ambient temperature  $T_{amb} = T_{boil} = 447$  K to the droplet initial temperature  $T_{d,0} = 315$  K at the droplet surface. As time goes by, the temperature inside the droplet increases, and the ambient fluid temperature decreases correspondingly. The numerical prediction agrees well with the analytical result, with a relative deviation of  $\delta_{error} \equiv |T_{num}(r, t) - T_{anal}(r, t)|/T_{anal}(r, t) < 0.01\%$ . This validation demonstrates the accuracy of the present model for the beginning of the droplet heating period.

#### 4.2.3. Vaporization of *n*-decane droplet in quiescent air

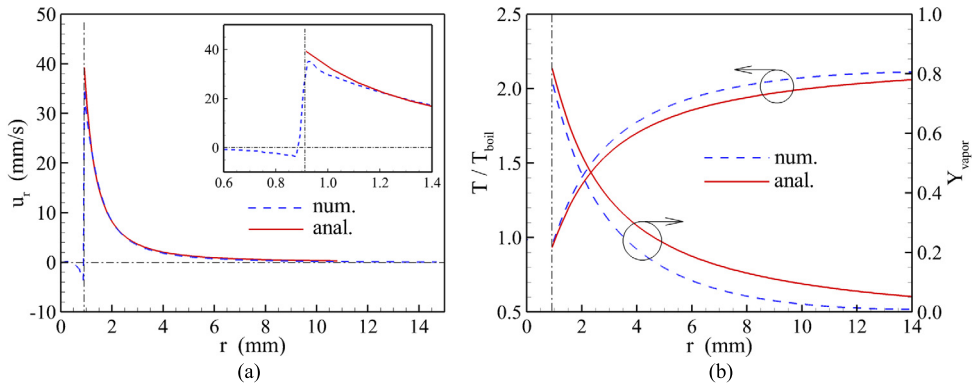
As part of our validation, we examine the vaporization of a single *n*-decane droplet in a quiescent air environment and validate the present model against the classical “ $D^2$ -law” [25]. An analytical solution of the droplet behavior can be obtained by solving the conservation equations of mass and energy with the uniform-property and quasi-steady-state assumptions [25]. The evolution of droplet diameter takes the following form, commonly known as the  $D^2$  law,

$$D^2 = D_0^2 - Kt \tag{25}$$

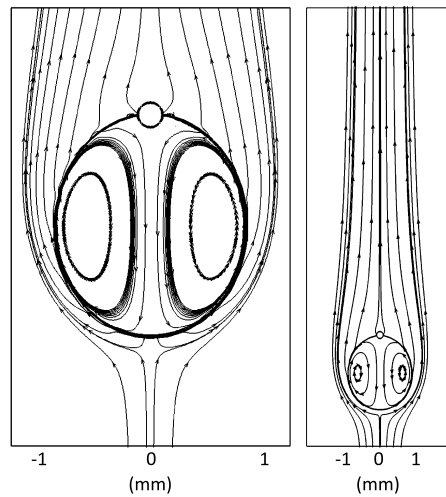
where  $K$  is a constant determined by the liquid and gas properties.

Fig. 6 shows a comparison between the numerically and analytically determined temporal evolution of the square of the droplet diameter. Two different methods were used to calculate the droplet diameter in the numerical simulation. The first is based on the volume of the liquid phase; the second involves the subtraction of the liquid volume of the evaporated liquid in the gas phase from the initial liquid volume. Two methods are used in order to examine the consistency between the mass of the evaporated liquid and that of the lost liquid. In the simulation, the evaporated liquid mass is calculated from  $t = 0$  to 2.5 s. Good agreement is obtained between the two methods. When  $t > 2.5$  s, the vapor spreads out of the simulation domain. At this point the vapor mass estimate is no longer correct, and the two values of evaporated mass diverge. Compared with the analytical solution, the slopes of the numerical results are slightly higher in the initial period. This is caused by the initial condition of the numerical simulation;  $Y_{vap} = 0$  and  $T_{gas} = 1000$  K everywhere in the gas phase. The vaporization rate is thus slightly higher than in the quasi-steady state. The droplet diameter square  $D^2$  decreases from 3.92 to 1.8 mm<sup>2</sup> at the end of the simulation.

Fig. 7 shows the distributions of radial velocity, temperature, and mass fraction in the gas phase at  $t = 1$  s. The radial velocity profiles exhibit good agreement between the numerical and analytical results throughout the gas phase, except in



**Fig. 7.** Numerical and analytical results at  $t = 1$  s for  $n$ -decane droplet vaporization in quiescent air: (a) Spatial distribution of radial velocity; (b) Spatial distributions of normalized temperature and vapor mass fraction.



**Fig. 8.** Flow patterns of an  $n$ -decane droplet suspended in a uniform air flow at  $t = 1$  s,  $U_{gas} = 1$  m/s.

the source layer near the droplet surface. The small deviation in the source layer is caused by the representation of the physical reality of the infinitely thin interface, where the vaporization takes place, by a source layer of finite thickness. This problem can be mitigated, but not obviated, by increasing the grid resolution near the interface and decreasing the thickness of the source layer.

Fig. 7(b) shows comparisons of the normalized temperature and vapor mass fraction in the gas phase. At the droplet surface, the numerically predicted temperature is  $(T_s/T_{boil})_{num} = 0.942$ , which is slightly (0.75%) higher than the analytical value of  $(T_s/T_{boil})_{anal} = 0.935$ . The numerically predicted vapor mass fraction is  $(Y_{vap})_{num} = 0.78$ , which is 4.88% smaller than its analytical counterpart  $(Y_{vap})_{anal} = 0.82$ . The noticeable decrease in vapor mass fraction in the simulation is primarily attributed to the finite thickness of the interfacial layer where the vaporization takes place. The situation can be improved by decreasing the source layer thickness. In the gas phase, deviations are observed in both the temperature and vapor mass fraction profiles, probably due to the use of the quasi-steady-state assumption in the analytical solution. The quasi-steady-state assumption requires that the time scale for interface regression be much larger than that for heat and mass transfer, a condition not satisfied in the present case.

#### 4.2.4. Vaporization of $n$ -decane droplet in uniform air flow

The vaporization of an  $n$ -decane droplet in a hot, uniform air flow is treated, mimicking the experiment of Wong and Lin [24]. The fluid properties are listed in Table 1. The air flow velocity is  $U_{gas} = 1$  m/s. The Reynolds number based on the initial droplet diameter and velocity is  $Re_d = U_{gas}D_0/\bar{\nu}_{gas} = 42.9$ . The droplet remains largely spherical throughout its lifetime. Liquid expansion is not considered in the simulation because of the constant-density assumption, and this will introduce deviation from the experimental result in the initial heating period [19]. The simulation domain of  $L \times H = 200R_0 \times 20R_0$ , where  $R_0$  is the initial droplet radius, is sufficiently big to render the boundary influence negligible. Outflow conditions are implemented at the spanwise and downstream boundaries.

Fig. 8 shows typical flow patterns illustrated by the streamlines at  $t = 1$  s. The flow inside the droplet is characterized by an axisymmetric recirculating flow, which transfers heat from the droplet surface to the interior. Outside the droplet, the

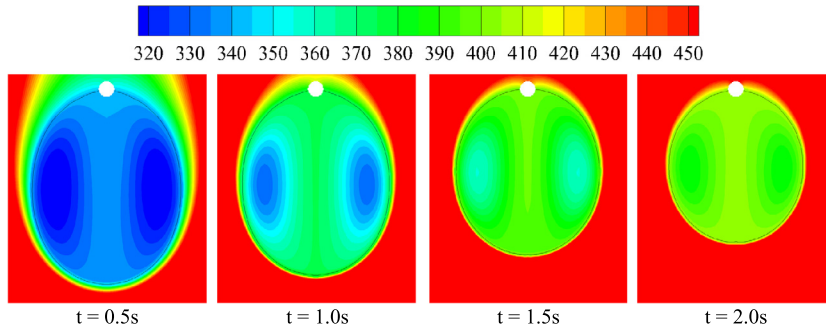


Fig. 9. Evolution of temperature of an *n*-decane droplet suspended in a uniform air flow at  $U_{gas} = 1$  m/s.

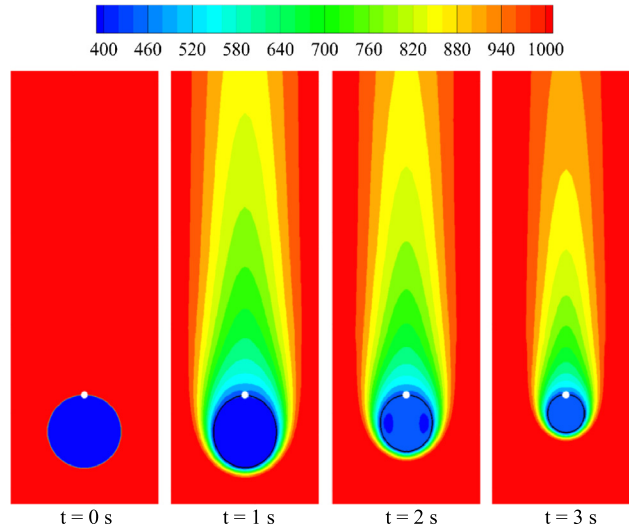


Fig. 10. Evolution of temperature around an *n*-decane droplet suspended in a uniform air flow at  $U_{gas} = 1$  m/s.

Stefan flow created by the evaporated liquid forms an envelope around the droplet and separates the outer air flow from the droplet. The interface between the outer air flow and the inner Stefan flow provides space for chemical reactions in the case of liquid fuel combustion.

A droplet initially at low temperature is first heated by the ambient hot air. At this stage, the heat from the hot air is mostly transferred to the interior of the droplet, and the interface temperature  $T_s$  and the vaporization rate  $\dot{m}''$  are relatively low. Fig. 9 shows the temperature evolution in the droplet from  $t = 0.5$  to 2.0 s. A certain fraction of the heat transferred to the droplet goes to evaporate liquid to vapor, and the remainder is absorbed by the droplet and increases its interior temperature. The recirculating flow within the droplet acquires heat from the interface through diffusion, and then advects the heat to the interior.

As the droplet temperature increases, the heat transfer to the droplet interior is reduced, and the surface vaporization rate  $\dot{m}''$  increases. Figs. 10 and 11 show the evolution of the temperature and vapor mass fraction, respectively, from  $t = 0$  to 3 s. In this period, the droplet size decreases from its initial value of 1.98 mm to 0.99 mm. The thermal and mass boundary layers on the upwind surface can be clearly identified.

Fig. 12 compares the numerical prediction with the experimental measurement of Wong and Lin [24] in terms of the temporal variation of the droplet temperature and diameter. The overall process can be divided into the droplet heating and vaporization stages. In the early period, the heat transferred to the droplet is mostly absorbed by the droplet, increasing the droplet temperature, and the vaporization rate is low. As the droplet heats up, the vaporization rate increases. Once the droplet surface temperature reaches its pseudo wet-bulb state, further heating is primarily consumed as phase change, and significant vaporization takes place.

The variation of the temperature at the droplet center,  $T_c$ , is shown in Fig. 12(a). In the heating stage ( $t < 1.5$  s), the numerical prediction agrees well with the experimental measurement. When  $t > 1.5$  s, the droplet temperature approaches a constant value asymptotically. The predicted temperature is slightly lower than the experimental values. The relative error  $\delta_{error,T} \equiv |T_{d,num} - T_{d,exp}|/T_{d,exp}$  is 2.42%; this difference could be attributable to measurement uncertainty and/or the representation of the droplet surface where the mass transfer takes place by source/sink layers of finite thickness. The latter could be improved by increasing the grid resolution near the droplet surface.

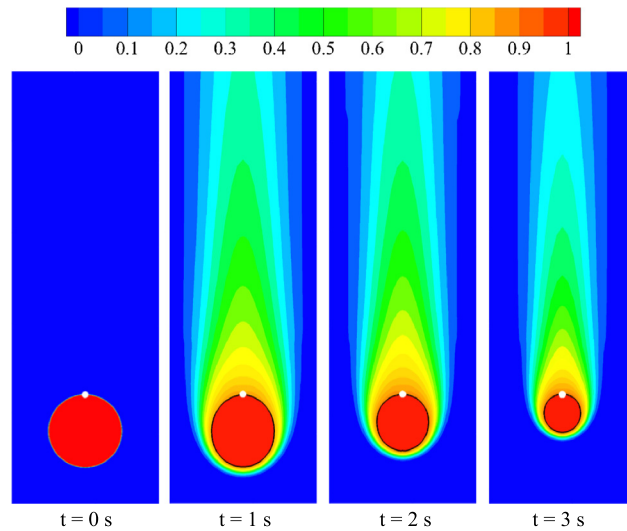


Fig. 11. Evolution of vapor mass fraction around an *n*-decane droplet suspended in a uniform air flow at  $U_{gas} = 1$  m/s.

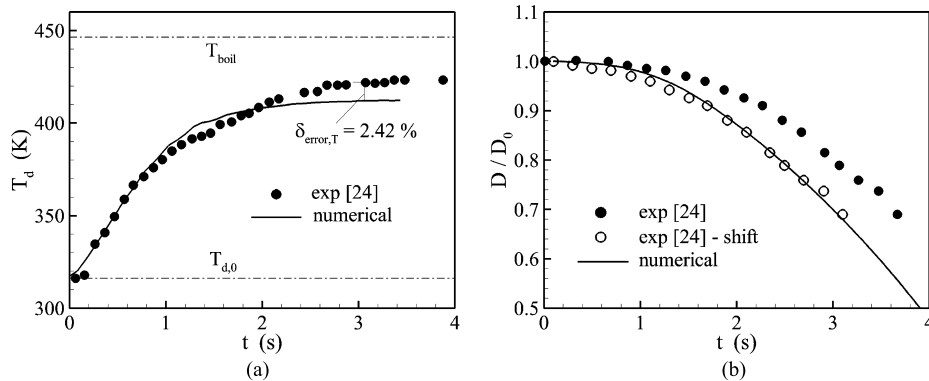


Fig. 12. Evolution of temperature at droplet center  $T_c$  and droplet diameter for *n*-decane droplet suspended in a uniform air flow: (a) Temperature at droplet center; (b) Droplet diameter.

The temporal variation of droplet diameter is shown in Fig. 12(b). In the initial droplet heating stage, the size evolution proceeds at a much lower rate than in the vaporization stage. The decrease in the calculated droplet size is faster than its experimental counterpart. As pointed out by Strotos et al. [26], the primary reason for such deviation is that the liquid thermal expansion in the heating stage is not considered in the numerical model, in which the incompressible flow assumption holds. The slope of the decrease in size, however, is the same as that of the experimentally measured values; this is demonstrated by shifting the experimentally measured values back to the end of the heating stage. The solid curve (numerical prediction) and the circles (shifted experimental measurements) demonstrate good agreement.

The droplet evolution shown in Fig. 12 suggests that the time scales of the heating and vaporization stages are comparable. In real combustion devices, liquid fuel is generally preheated to a high temperature before being injected into the chamber to improve the combustion efficiency. In such a pre-heated case, the initial droplet temperature is close to the final constant temperature; here we consider a simulation with all the parameters the same as in the above case, but we ignore the heat transfer inside the droplet. Fig. 13 shows a comparison of the droplet diameter evolution. The solid dots represent original experimental data. As in Fig. 12(b), the experimental data are shifted horizontally to the left and represented by circles to compare with the numerical result. The consistency of the curve slopes in this figure demonstrates good agreement between the numerical prediction and experimental measurement in terms of the droplet regression rate.

In this simulation we also examine the mass of the evaporated fuel in the gas and the mass lost from the liquid phase. Fig. 14 compares the droplet diameter calculated based on the liquid volume (Method 1) with that obtained by subtracting the liquid volume of the evaporated fuel from the initial liquid volume (Method 2). Note that the mass of the evaporated fuel can only be accurately estimated before the vapor spreads out of the domain at about  $t = 0.1$  s. Results calculated using the two methods agree well, and the deviation is about 2.1%.

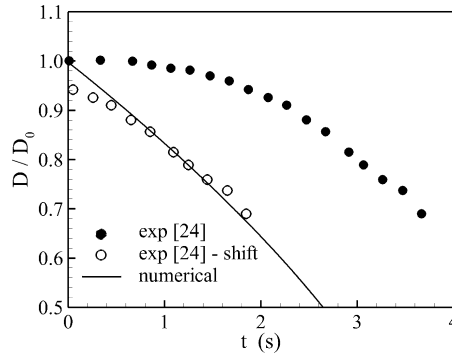


Fig. 13. Evolution of droplet diameter without consideration of heat transfer inside the droplet.

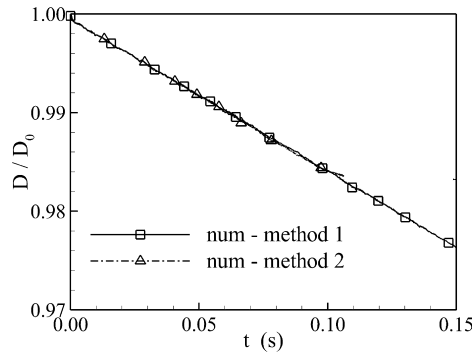


Fig. 14. Evolution of droplet diameter using two methods. Heat transfer inside the droplet is not considered.

#### 4.2.5. Vaporization of an impulsively started *n*-decane droplet at 1 atm in quiescent air

In order to demonstrate the robustness of the present model, we study the vaporization of an impulsively started droplet in quiescent hot air. With the increase in the droplet initial velocity, the aerodynamic force exerted on the droplet becomes stronger, leading to a more significant droplet deformation. When the velocity reaches a critical value, droplet breakup takes place. The droplet deformation and breakup modes can be characterized by two non-dimensional parameters: the Weber and the Ohnesorge numbers [27,28], which are defined as  $We \equiv \bar{\rho}_{gas} U_0^2 D_0 / \sigma$  and  $Oh \equiv \mu_l / \sqrt{\rho_l D_0 \sigma}$ , respectively. Here  $\sigma$  is the surface tension. In general, the time scales of droplet motion and deformation are smaller than that of droplet heating. All the parameters are identical to those of the above case of a single droplet suspended in a hot air flow, except for the droplet velocity. To focus on the vaporization of a deformed droplet, we ignore the heat transfer inside the droplet and assume that the droplet has been preheated to the final constant temperature when it starts to move at  $t = 0$  s. At  $t = 0$  s, the *n*-decane droplet with an initial temperature equaling the pseudo wet-bulb temperature starts to move at an initial droplet velocity  $U_0$  in quiescent hot air at  $T_{air} = 1000$  K. The droplet then decelerates, deforms, and evaporates as it moves. The simulation covers a spatial domain of 0.2 m, about 100 times the droplet diameter. Three different initial velocities  $U_0 = 1, 2, 5$  m/s are considered. The droplet has limited deformation for  $U_0 = 1$  and 2 m/s. Significant deformation takes place for  $U_0 = 5$  m/s.

Fig. 15 shows the time evolution of droplet deformation and vapor mass fraction for  $U_0 = 5$  m/s. The corresponding Reynolds number is  $Re_d = 214.5$ . The Weber number and Ohnesorge number are  $We = 5.22$  and  $Oh = 1.89 \times 10^{-3}$ , respectively. According to the regime diagram developed by Hsiang and Faeth [27], droplet deformation in this case is subject to periodic oscillation, and this is consistent with the deformation pattern observed in Fig. 15. Strotos et al. [29] have demonstrated that the heating and evaporation processes have little effect on droplet deformation due to the disparities in time scales.

Fig. 16 compares the temporal evolution of droplet position and diameter at different initial velocities. Because of the drag force by ambient air, the droplet velocity decreases slightly with time and causes curved trajectories. The evolution of droplet diameter shown in Fig. 16(b) indicates that the regression rate  $d(D/D_0)/dt$  increases with increasing droplet velocity  $U_0$ . When  $U_0$  increases from 1 to 2 m/s and from 2 to 5 m/s, the change in  $d(D/D_0)/dt$  becomes smaller and smaller. The dependence of the droplet regression rate on  $U_0$  decreases with increasing  $U_0$ . No experimental or theoretical studies of droplet vaporization with deformation are currently available in the literature for comparison, but the numerical results shown here demonstrate the expected trend in droplet vaporization rate. The present model could be effectively used to study two-phase flows with large deformation and high mass transfer rate.

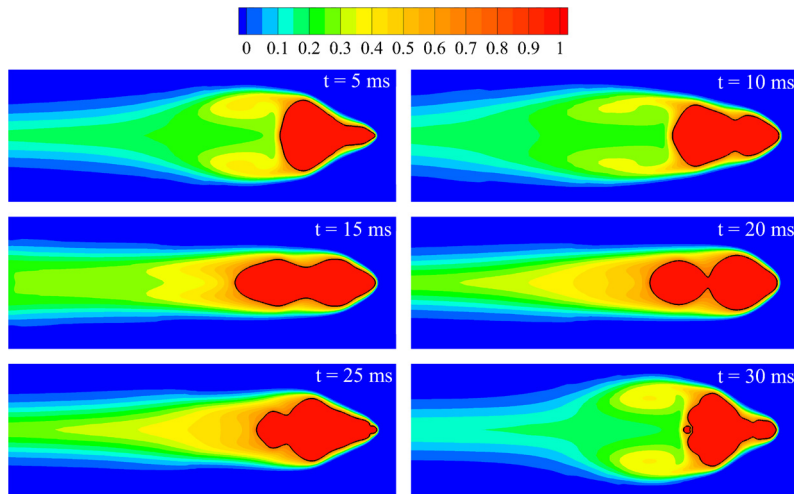


Fig. 15. Temporal evolution of vapor mass fraction for an impulsively started  $n$ -decane droplet in quiescent air,  $U_0 = 5$  m/s.

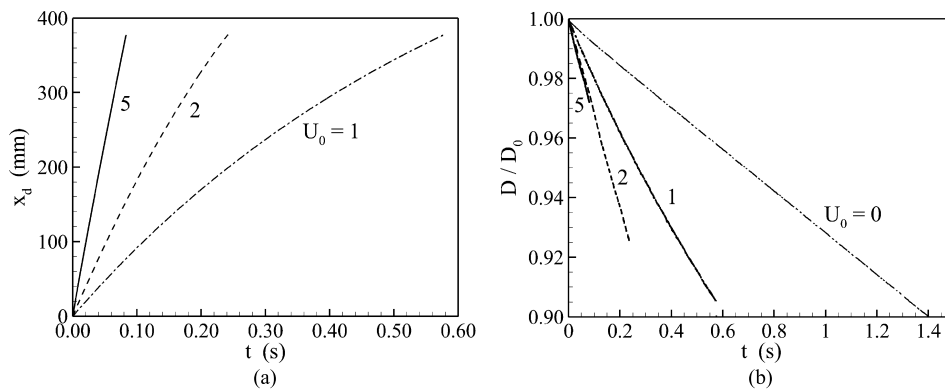


Fig. 16. Temporal evolution of droplet (a) position and (b) diameter for an impulsively started  $n$ -decane droplet in quiescent air.

#### 4.2.6. Vaporization of an impulsively started $n$ -decane droplet at 10 atm in quiescent air

In order to demonstrate the robustness of the present vaporization model, we studied the vaporization of an impulsively started  $n$ -decane droplet in quiescent air at 10 atm. The initial droplet diameter is  $D_0 = 0.1$  mm. The starting velocity of the droplet is  $U_0 = 10$  m/s. The ambient air temperature is 1000 K. The heat transfer inside the droplet is ignored. Under this condition, the density ratio of liquid to gas is  $\rho_{\text{liq}}/\rho_{\text{gas}} = 52.65$ , much smaller than that at 1 atm. The aerodynamic force on the droplet is strong enough to cause large deformation of the droplet. The Reynolds number is  $Re_d = 170.18$ . The Weber number and Ohnesorge number are  $We = 18.12$  and  $Oh = 5.68 \times 10^{-3}$ , respectively. According to the regime diagram of Hsiang and Faeth [27], the droplet deformation at these  $We$  and  $Oh$  is subject to the bag breakup mode. Fig. 17 shows the time sequence of droplet deformation and the vapor mass-fraction field. The characteristics of bag breakup are observed, consistent with the deformation patterns obtained in the simulation of Han and Tryggvason [30] in similar parameter ranges. The vortex ring behind the droplet recirculates the vapor in the droplet wake. Fig. 17 offers a reasonable prediction of the vaporization process of a moving droplet with large deformation. Since no experimental or theoretical results are available in the literature for comparison, the processes of vaporization of a moving droplet with large deformation have not yet been quantified, but the robustness of the presented model is demonstrated here.

## 5. Conclusions

A new approach based on decomposed vaporization mechanisms has been developed to treat the vaporization of a liquid droplet with large deformation and high mass transfer rate. In this model the mass transfer and resultant velocity jump at the two-phase interface are expanded over body-fitted source and sink layers of finite thickness. The treatment effectively preserves the advantages of well-developed interface localization methods and efficiently reduces the uncertainty and complexity caused by the combined treatments of mass/heat transfer and surface localization. The model does not depend on any specific interface localization methods and can be easily incorporated into any of them. With careful adjustment, the

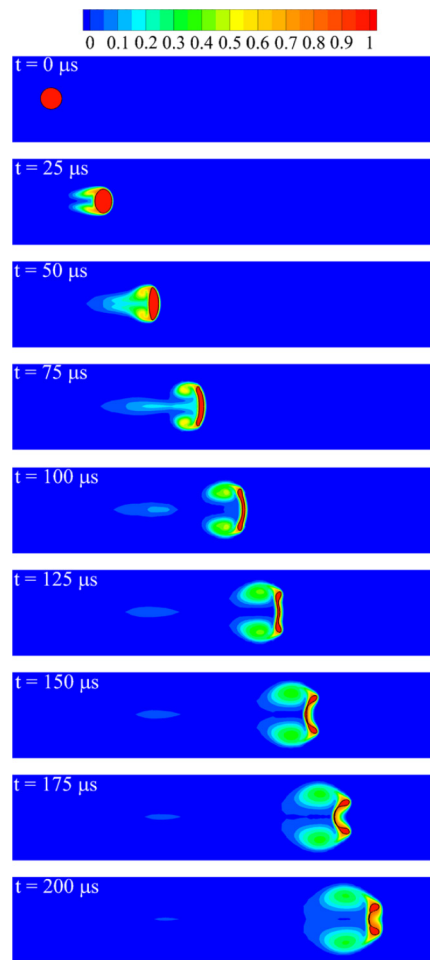


Fig. 17. Temporal evolution of vapor mass fraction for an impulsively started *n*-decane droplet in quiescent air,  $D_0 = 0.1$  mm,  $P_0 = 10$  atm,  $U_0 = 10$  m/s.

model could be extended to comprehensive models taking into account flow compressibility and chemical reactions in the gas phase.

The vaporization model is implemented into the VOF based code “Gerris.” As a model validation effort, a series of numerical simulations were conducted to study two-phase flow with mass transfer under different conditions. Good agreement with analytical predictions and experimental measurements demonstrate the efficiency and robustness of the present model in dealing with droplet vaporization over a broad range of density ratios and deformation in convective environments.

### Acknowledgements

This work was partly sponsored by the US Army Research Office under the Multi-University Research Initiative under Contract No. W911NF-08-1-0124, and partly by the William R. T. Oakes Endowment of the Georgia Institute of Technology. Special thanks are due to Stéphane Popinet for allowing us to use his work on the VOF and AMR algorithms.

### References

- [1] C. Hirt, B. Nicholls, Volume of fluid (VOF) method for the dynamics of free boundaries, *J. Comput. Phys.* 39 (1981) 201.
- [2] V.R. Gopala, B.G.M. van Wachem, Volume of fluid methods for immiscible-fluid and free-surface flows, *Chem. Eng. J.* 141 (2008) 204.
- [3] M. Sussman, P. Smereka, S. Osher, A level set approach for computing solutions to incompressible two-phase flow, *J. Comput. Phys.* 114 (1994) 146.
- [4] D. Peng, B. Merriman, S. Osher, H. Zhao, M. Kang, A PDE-based fast local level set method, *J. Comput. Phys.* 155 (1999) 410.
- [5] S. Unverdi, G. Tryggvason, A front-tracking method for viscous, incompressible, multi-fluid flows, *J. Comput. Phys.* 100 (1993) 25–37.
- [6] G. Tryggvason, B. Bunner, A. Esmaeili, D. Juric, N. Al-Rawahi, W. Tauber, J. Han, S. Nas, Y.J. Jan, A front-tracking method for the computations of multiphase flow, *J. Comput. Phys.* 169 (2001) 708.
- [7] S. Welch, J. Wilson, A volume of fluid based method for fluid flows with phase change, *J. Comput. Phys.* 160 (2000) 662–682.
- [8] T. Sato, R.T. Jung, S. Abe, Direct simulation of droplet flow with mass transfer at interface, *Trans. Am. Soc. Mech. Eng.* 122 (2000) 510–516.
- [9] J. Schlottke, B. Weigand, Direct numerical simulation of evaporating droplets, *J. Comput. Phys.* 227 (2008) 5215–5237.
- [10] G. Son, V.K. Dhir, Numerical simulation of film boiling near critical pressures with a level set method, *J. Heat Transf.* 120 (1998) 183–192.

- [11] F. Gibou, L. Chen, D. Nguyen, S. Banerjee, A level set based sharp interface method for the multiphase incompressible Navier-Stokes equations, *J. Comput. Phys.* 222 (2007) 536–555.
- [12] D. Juric, G. Tryggvason, Computations of boiling flows, *Int. J. Multiph. Flow* 24 (1998) 387–410.
- [13] A. Esmarelli, G. Tryggvason, Computations of film boiling. Part I: numerical method, *Int. J. Heat Mass Transf.* 47 (2004) 5451–5461.
- [14] S. Hardt, F. Wondra, Evaporation model for interfacial flows based on a continuum-field representation of the source terms, *J. Comput. Phys.* 227 (2008) 5871–5895.
- [15] G. Strotos, M. Gavaises, A. Theodorakakos, G. Bergeles, Numerical investigation of the evaporation of two-component droplets, *Fuel* 90 (2011) 1492–1507.
- [16] S. Popinet, Gerris: a tree-based adaptive solver for the incompressible Euler equations in complex geometries, *J. Comput. Phys.* 190 (2003) 572–600.
- [17] S. Popinet, An accurate adaptive solver for surface-tension-driven interfacial flows, *J. Comput. Phys.* 228 (2009) 5838–5866.
- [18] M.C. Yuen, L.W. Chen, On drag of evaporating liquid droplet, *Combust. Sci. Technol.* 14 (1976) 147–154.
- [19] K.C. Hsieh, J.S. Shuen, V. Yang, Droplet vaporization in high-pressure environments I: near critical conditions, *Combust. Sci. Technol.* 76 (1991) 111.
- [20] B. Abramzon, W.A. Sirignano, Droplet vaporization model for spray combustion calculations, *Int. J. Heat Mass Transf.* 32 (1989) 1605–1618.
- [21] X. Chen, D. Ma, V. Yang, S. Popinet, High-fidelity simulations of impinging jet atomization, *At. Sprays* 23 (2013) 1079–1101.
- [22] X. Chen, V. Yang, Thickness-based adaptive mesh refinement methods for multi-phase flow simulations with thin regions, *J. Comput. Phys.* 269 (2014) 22–39.
- [23] X. Chen, V. Yang, Recent advances in physical understanding and quantitative prediction of impinging-jet dynamics and atomization, *Chin. J. Aeronaut.* 32 (1) (2019) 45–57.
- [24] S.C. Wong, A.C. Lin, Internal temperature distributions of droplets vaporizing in high-temperature convective flows, *J. Fluid Mech.* 237 (1992) 671–687.
- [25] S.R. Turns, *An Introduction to Combustion—Concepts and Application*, McGraw-Hill, New York, 1996.
- [26] G. Strotos, I. Malgarinos, N. Nikolopoulos, M. Gavaises, Predicting the evaporation rate of stationary droplets with the VOF methodology for a wide range of ambient temperature conditions, *Int. J. Therm. Sci.* 109 (2016) 253–262.
- [27] L.P. Hsiang, G.M. Faeth, Drop deformation and breakup due to shock wave and steady disturbances, *Int. J. Multiph. Flow* 21 (1995) 545–560.
- [28] P. Khare, D. Ma, X. Chen, V. Yang, Phenomenology of Secondary Breakup of Newtonian Liquid Droplets, *AIAA Paper* 2012-0171, 2012.
- [29] G. Strotos, I. Malgarinos, N. Nikolopoulos, M. Gavaises, Numerical investigation of aerodynamic droplet breakup in a high temperature gas environment, *Fuel* 181 (2016) 450–462.
- [30] J. Han, G. Tryggvason, Secondary breakup of axisymmetric liquid drops. II. Impulsive acceleration, *Phys. Fluids* 13 (2001) 1554–1565.